Available online at www.sciencedirect.com
ScienceDirect
Mathematics and Computers in Simulation 215 (2024) 184–207
MATHEMATICS AND COMPUTERS IN SIMULATION
www.elsevier.com/locate/matcom

Original articles

Simulating spectral images of natural waters and submerged objects from a bird's-eye view

Andrew Corbett[a,*], Jacqueline Christmas[a], Christopher Lawrence[b], Joseph Feenan[b]

[a] *Department of Computer Science, University of Exeter, Exeter, EX4 4RN, UK*
[b] *QinetiQ, Cody Technology Park, Ively Road, Farnborough, GU14 0LX, UK*

Received 19 October 2022; received in revised form 13 July 2023; accepted 28 July 2023
Available online 7 August 2023

Abstract

We describe a new approach to modelling two-dimensional 'bird's-eye' images of natural waters, sensitive to the spectral absorption and scattering over the visual range. Constructed using the mathematical framework of invariant imbedding to efficiently and economically resolve the associated radiative transfer equations, this method provides a fast routine to build physically accurate simulations. We characterise the quality of the water through surface chlorophyll content, instead of the traditional Jerlov water types. Simulations of 'Macbeth' colour identification chart at different depths are compared with real, hyperspectral images recorded in a tank.

Keywords: Radiative transfer; Optical oceanography; Invariant imbedding

1. Introduction

The venture of building digital simulations of natural phenomena is vast and multifaceted–not to mention difficult–but with great dividend returned to the motivating problems. Oceanographic phenomena are amongst the most complex, given the complexity of atmospheric systems, but also the difficulty in acquiring the numerous data required to describe specific scenarios. Nevertheless, the need for developing accurate, realistic and encompassing digital twins is greatly sought after in industry and scientific research alike. Spectral imaging of underwater objects from a bird's-eye point of view has important applications to coastal depth mapping [4,18]; underwater microplastic detection [15]; general detection of man-made objects via a colour criterion [2]. Such systems would be relevant for practical uses such as search and rescue analysis or early maritime warning systems. But also academically, many machine learning and artificial intelligence models require large volumes and a wide variety of training data, which is challenging to collect in the maritime environment. The simulation technique provided here is able to generate realistic training data for such machine learning models.

In this work, we address the task of simulating the optical output of a natural water body containing submerged anomalies of different colour at various depths. The model we develop is designed to generate the resultant bird's-eye view over a two-dimensional water surface in full spectral resolution in the visual range. Our model, which we call

* Corresponding author.
E-mail address: a.j.corbett@exeter.ac.uk (A. Corbett).

https://doi.org/10.1016/j.matcom.2023.07.025

Fig. 1. Sunken cross-shaped object with Lambertian reflectance (dry colour displayed in top-right) at a depth of 2.5 m in chlorophyll-free water.

'`bird5eye`', provides a significant step in the use of physical models to create physically accurate digital twins of maritime scenarios; an example output of which is given in Fig. 1.

Our `bird5eye` model builds on the approach of [23], in that we solve the depth-continuous radiative transfer equation–the "equation of motion" for spectral light distributions–using the technique of *invariant imbedding* [1,3]. We extend this to the two-dimensional case to derive a computationally tractable solution for bird's-eye views. Key novelties of our approach include the introduction of new *theoretical* variants on the approach of [23], described in Section 1.2; and a new proposal and implementation of water-type parameterisation, that is the measure of water quality. This later proposal is based on using surface chlorophyll *alone* as an indicator of the deep chlorophyll profile [36] and hence the determinant of the Inherent Optical Properties (IOPs) of a given water body [25]. This is positioned as a practical alternative to the usual practice of using the somewhat less empirical 'Jerlov types', based on ambiguous historical readings [17]; see also [24].

We draw contrast with other physically-accurate simulation procedures using Monte Carlo algorithms [9,21] which, whilst successful in prediction, are far too computationally expensive to generate two-dimensional systems in a tractable time. The world of rendering methods in computer graphics also offers rudimentary approaches to simulate seawater, some with in built physical considerations (such as the exponential decay of radiance); see [10] for a detail survey. However, the combination of physical precision in the present work (inherited from [25]) and the fast-compute mathematical structure (see Section 4) position our model for utilisation for real-life graphical oceanographic simulation and experimentation.

1.1. Modelling chlorophyll water types in practice

It has recently been shown [25] that in many deep water environments, the physical parameters governing the absorptive and scattering properties depend explicitly on a single determinant: chlorophyll concentration. The state-of-the-art methodology [25] states that chlorophyll concentration, as a function of depth, may be used as a fundamental parameter to govern the IOPs of the water body. Moreover, in a recent exploratory study [36], it was shown that chlorophyll profile may be reasonably predicted in terms of surface chlorophyll concentration; this results in a natural distinction of chlorophyll strata, the 'Uitz classification'. We incorporate this classification [36] into our model, with the ambition to use `bird5eye` to prove experimentally that surface chlorophyll concentration is

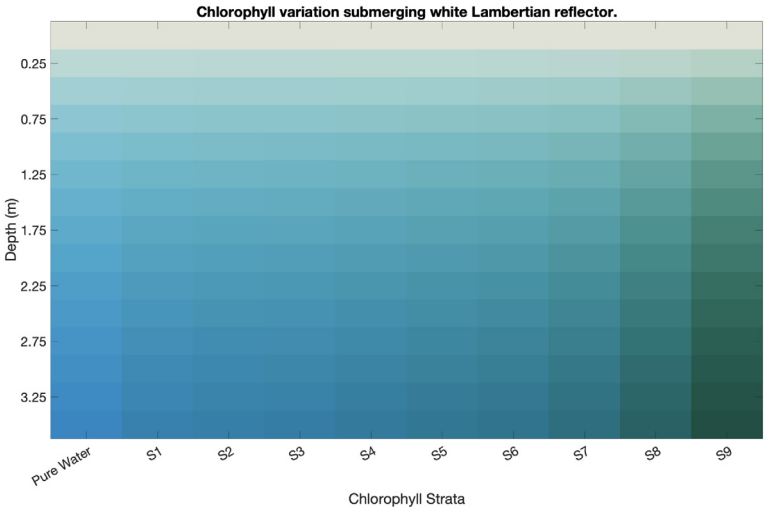

Fig. 2. A `bird5eye` prediction of surface colour upon submerging a white Lambertian reflector (see depth 0 m) to 3.5 m, recording every 0.25 m in the vertical axis. The horizontal axis varies through the chlorophyll strata in the Uitz classification.

an accurate predictor of sea type from a surface-imaging perspective. We propose that this practice replaces the traditional Jerlov type classification [17,34] as a more accurate alternative, whilst remaining coarse enough to apply generally and quickly. A colour variation example predicted by our model is illustrated in Fig. 2 where we submerge a white Lambertian reflector in each of the chlorophyll strata proposed by [36].

1.2. Theoretical developments

The catalyst for our contribution is the extension of the one-dimensional modelling approach of [23] to a bird's-eye projection of a three-dimensional plane-parallel water body. The theoretical tool by which we solve the associated radiative transfer equation is the method of invariant imbedding (see Appendix E); first introduced to describe propagation through stellar atmospheres [1], this approach has been applied successfully to oceanography [23], engineering [3] and more recently to deep neural networks [8]. To solve the three-dimensional radiative transfer equation directly is a computationally intractable problem. It is posed as a coupled, three-dimensional system of non-linear PDEs for which numerical solvers are unfit to determine with computational efficiency. But taking a modular approach, facilitated by the invariant imbedding method, `bird5eye` performs one-dimensional calculations and distributes these over a three-dimensional geometry, incorporating boundary conditions locally.

We also introduce further theoretical improvements in our model's mathematical structure: efficient (complex) Fourier decoupling, allowing for multicore parallel processing of Fourier coefficients; and a linear system-based inelastic scattering solution, alongside repeated monochromatic runs where each scalar wavelength is fixed, the inelastic solution is found in an iterative fashion. See Section 3, accompanied by Appendices B, and F, respectively.

1.3. Experimentation

We implement our `bird5eye` model in Matlab, a scientific computing platform, where we perform the back-end computations. This is then connected to a user interface to facilitate ease of simulations.

To road-test the outputs of our model, we have conducted an image collection experiment in which a colour identification chart (known colloquially as a Macbeth chart), with known spectral reflectances [27], is submerged in a water tank in a controlled environment. Images are taken at regular intervals on a hyper-spectral camera, allowing for real-life comparison with the model's predictions at high spectral resolution. See Section 6 and Fig. 7. Whilst taking measurements out at sea is a difficult and expensive task, we hope to explore experimentation with chlorophyll types in real deep-sea environments.

1.4. Organisation of results

In Section 3 we give background to the transfer of radiation in natural waters and set out the mathematical structure on which `bird5eye` is built. Our discrete solution, both with respect to the Fourier decomposition and wavelength analysis, is inspired by but different from past frameworks [23]. In Section 4 we generalise this result to derive the bird's-eye view solution, the key result of our work. In Section 5 we describe our results on a Chlorophyll classification of ocean waters, to improve upon the legacy 'Jerlov types'. Then in Section 6 we exhibit our experimental results that support our theoretical model.

2. Index of acronyms

The following are commonly used throughout the text. We indicate where there first use and definition can be found.

- RTE: Radiative Transfer Equation; see Section 3.
- VSF: Volume Scattering Function; see Section 3.
- IOP: Inherent Optical Property; see Section 3.1.
- CDOM: Coloured Dissolved Organic Matter; see Section 3.1.1.
- IVP: Initial Value Problem; see Section 4.

3. Solving the radiative transfer equation

Our primary goal is to solve the plane-parallel Radiative Transfer Equation (RTE) as a two-point boundary value problem for a range of water types. We solve for the radiance, a directional and spectral distribution of output radiative power as a given point in space, here denoted by $L(z;\mathbf{r})$, dependent on the depth variable z, with $z=0$ at the mean sea surface and increasing into the water, and a direction, with respect to the location of the value $L(z;\mathbf{r})$, given by the unit vector $\mathbf{r}$. The RTE is an integro-differential equation of the form

$$\mu\frac{dL}{dz}(z;\mathbf{r}) = -c(z)L(z;\mathbf{r}) + \int_{\mathcal{B}} L(z;\mathbf{r}')\beta(z;\mathbf{r}'\to\mathbf{r})d\mathbf{r} + \sigma(z;\mathbf{r}) \tag{1}$$

where $c(z) = a(z) + b(z)$ is the beam attenuation coefficient, a sum of absorption and scattering coefficients, respectively; β is the (elastic) Volume Scattering Function (VSF), describing scattering processes between directions $\mathbf{r}'$ and $\mathbf{r}$; σ is an external source term; and finally the geometric distribution is parameterised by the unit ball

$$\mathcal{B} = \{(\mu,\phi)\,|\,\mu\in[-1,1],\ \phi\in[0,2\pi)\} \tag{2}$$

where μ is the polar coordinate, aligned with the z-axis so that $\mu=+1$ points into the water, and ϕ is the planar azimuth, whose origin is taken relative to the non-homogeneous surface boundary and incident radiation. See Fig. 3 for a graphical depiction of the geometrical set-up.

Radiance also depends on the spectrum of wavelengths λ. For brevity, in (1) we describe the inelastic RTE and consider the monochrome radiance dependent on a fixed wavelength λ. Indeed, the variables a, b, c, β and σ each have a suppressed dependence on λ. In Appendix F, we give a general elastic solution contained in the `bird5eye` implementation.

Attached to the RTE are boundary conditions at the surface and bottom. These are given explicitly in Appendix C and used in the framework in Section 4. The IOPs a, b, c, and β are described in Section 3.1.

3.1. Inherent optical properties

The calibration of `bird5eye` is based on state-of-the-art experimental measurements for non-coastal waters, which we log here. These waters fall into Jerlov's categorisation I–III [17,34] and cover 95% of the earths waters. We exclude Jerlov coastal types 1C-9C. The relevant IOPs are comprised of the absorption $a(z)$ and scattering $b(z)$ coefficients as well as the VSF $\beta(z;\mathbf{r}'\to\mathbf{r})$, see Section 3.1.3. Most importantly, we observe that for fixed wavelengths λ the coefficients a and b have an explicit functional dependence on chlorophyll concentration $\mathrm{Chl}(z)$ at depth z. Consequently, the same is also true for the VSF by a separation of variables (see later in Eq. (6)), thus implying $\mathrm{Chl}(z)$ is a determining factor for all IOPs present in (1).

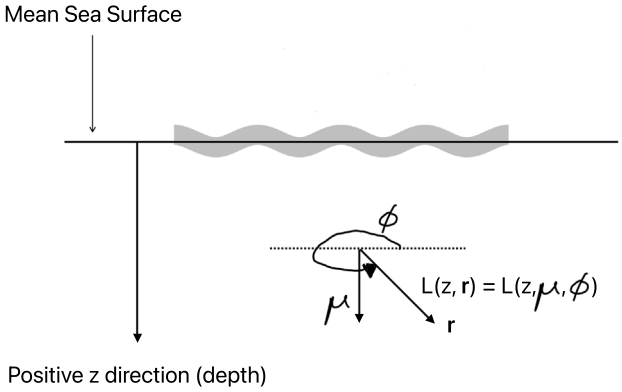

Fig. 3. Geometry for theoretical radiative transfer construction.

Whilst the below data are implemented into our out-of-the-box model, we have also implemented various other IOP classification into `bird5eye`, and we stress that for high precision, the IOPs for the given water under analysis should be used.

3.1.1. Absorption coefficients

Recalling the wavelength dependence here, following [23,34] we decompose the absorption coefficient into three parts:

$$a(z, \lambda) = a_{\mathrm{w}}(\lambda) + a_{\mathrm{Chl}}(z, \lambda) + a_{\mathrm{CDOM}}(z, \lambda) \tag{3}$$

with the factors describing the absorption due to pure water, chlorophyll and Coloured Dissolved Organic Matter (CDOM), respectively.

For pure water, we define $a_{\mathrm{w}}(\lambda)$ for λ over 200–800 nm as follows: by the discussion of results in [32, §6], specifically concerning the measurements of [6], we use the values of $a_w(\lambda)$ as computed by [32] in the region 380–727.5 nm and extend these by the values recorded by [12] in the region 340–380 nm. We further assume the values of [33] to extend the data set in the regions 200–330 nm and 730–800 nm, referring to [32, Fig. 10] to justify this selection. We note in particular the mild divergence in this choice of $a_w(\lambda)$ with [34], who take an average of the data given in [6,28,32].

For absorption by chlorophyll (via phytoplankton) we use the model proposed by [5], with data made available from the 'A New IOP Model for Case 1 Water' tab of www.oceanopticsbook.info. For absorption by CDOM, we import a result of [34] which is a numerical deduction of the functional form of a_{CDOM} in terms of Chl at fixed depths z. The coefficient itself is written in functional form,

$$a_{\mathrm{CDOM}}(\lambda) = a_{\mathrm{Chl}}(440) M \exp(-\alpha(\lambda - 440)) \tag{4}$$

where the coefficients α and M are functions of Chl as in [34, Figs. 7 & 8], respectively.

3.1.2. Scattering coefficients

We follow the chlorophyll based model of [13] for which we have a similar decomposition to the absorption case but with only two summands:

$$b(z, \lambda) = b_{\mathrm{w}}(\lambda) + b_{\mathrm{p}}(z, \lambda) \tag{5}$$

where $b_{\mathrm{w}}(\lambda)$ is the well understood depth-invariant pure water scattering coefficient as given by [34, Eq. (8a)] and b_{p} is the particle scattering coefficient. For the latter we apply the formulation described by [26, Eq. (14)]. This is calibrated via [26, Eq. (8)] using the measurements of [22].

3.1.3. The volume scattering function

The angular distribution of scattering effects is well understood; we follow [23, Ch. 3]. Whilst the industry-standard experimental data dates back to [30], it matches well understood analytic models of [11,14] of which we include all of in our `bird5eye` implementation. See the 'Petzold's Measurements' tab of www.oceanopticsbook.info.

Analytically, we average over $\beta(z;(\mu',\phi')\to(\mu,\phi))$, as in [23, Eq. (3.5)] to define the scattering phase function $\tilde{\beta}$ via

$$\beta(z;(\mu',\phi')\to(\mu,\phi)) = b(z)\tilde{\beta}(\psi) \tag{6}$$

depending only on the scattering angle ψ between (μ',ϕ') and (μ,ϕ),

$$\cos(\psi) = \mu'\mu + \sqrt{(1-\mu'^2)(1-\mu^2)}\cos(\phi-\phi'), \tag{7}$$

and uniform over depth z. This in turn gives rise to well known symmetries of the VSF:

$$\begin{aligned}\beta(z;(\mu',\phi')\to(\mu,\phi)) &= \beta(z;(\mu',0)\to(\mu,\phi-\phi'))\\ &= \beta(z;(\mathrm{sgn}(\mu)\mu',\phi')\to(\mathrm{sgn}(\mu')\mu,\phi))\\ &= \beta(z;(\mu',\phi)\to(\mu,\phi'))\end{aligned} \tag{8}$$

where $\mathrm{sgn}(\mu) \coloneqq \mu/|\mu|$. We shall use these in our forthcoming analysis.

3.2. The discrete radiative transfer equation

For computer simulation, both the directional and spectral (wavelength) components require a discrete partitioning, where the components of (1) are averaged over the intermediate intervals. We follow [23, §4.7] with some minor variation. Wavelength averaging is considered in Appendix F.

To decompose the integral in (1) we fix integers N and M and approximate the unit ball $\mathcal{B}$ by a partition of quadrilateral facets, or 'quads'. We denote a quad by $\mathcal{Q}_{iu} = \mathcal{I}_i \times \mathcal{U}_u$ for $i = 1\dots M$ and $u = 1\dots N$ where the collections $\{\mathcal{I}_i\}_i$ and $\{\mathcal{U}_u\}_u$ partition $[0,1]$, and $[0,2\pi]$, respectively; we reflect the polar coordinates so that $\{\mathcal{I}_{-i}\}_i$ partitions $[-1,0]$. We pick representatives $\mu_i \in \mathcal{I}_i$, extended by $\mu_{-i} \coloneqq -\mu_i \in \mathcal{I}_i$, and $\phi_u \in \mathcal{U}_u$. We let $\tilde{\mu}_i$ denote the average of the endpoints of $\mathcal{I}_i$. We assume that the length of each $\mathcal{U}_u$ has equal length, in that $\int_{\mathcal{U}_u} d\phi = 2\pi/N$, and denote the length of $\mathcal{I}_i$ by $\Delta\mu_i \coloneqq \int_{\mathcal{I}_i} d\mu$. Then the solid angular volume of each quad is given by $\Delta\mathcal{Q}_{iu} \coloneqq \int_{\mathcal{Q}_{iu}} d\mu d\phi = \frac{2\pi}{N}\Delta\mu_i$. (See Appendix A.2 for the explicit partition used in `bird5eye`.)

We shall substitute functions $F:\mathcal{B}\to\mathbb{C}$ for their 'quad averaged' counterparts $F(i,u)$ normalised so that if $F(\mu,\phi) = 1$ then $F(i,u) = 1$ for $(\mu,\phi)\in\mathcal{Q}_{iu}$. We similarly average bi-variate functions $G:\mathcal{B}\times\mathcal{B}\to\mathbb{C}$ but normalise them such that if $G((\mu',\phi')\to(\mu,\phi)) = 1$ then $G((i',u')\to(i,u)) = \Delta\mathcal{Q}_{i',u'}$ for $(\mu',\phi')\in\mathcal{Q}_{jv}$. Explication of this process is described in Appendix A.3.

With this construction, we replace (1) with its quad-averaged analogue:

$$\begin{aligned}\tilde{\mu}_i\frac{dL}{dz}(z;i,u) = &-c(z)L(z;i,u)\\ &+\sum_{v=0}^{N}\sum_{j=\pm1}^{M}\beta(z;(j,v)\to(i,u))L(z;j,v)+\sigma(z;i,u).\end{aligned} \tag{9}$$

3.3. Spectral decoupling via the complex Fourier transform

We now change variables in (9) to instead consider the complex Fourier transforms

$$\hat{L}(z;i;\ell) \coloneqq \sum_{u=0}^{N-1} L(z;i,u)e(-\ell u/N);\ \ \hat{\sigma}(z;i;\ell) \coloneqq \sum_{u=0}^{N-1}\sigma(z;i,u)e(-\ell u/N); \tag{10}$$

and

$$\hat{\beta}(z;i,j;\ell) \coloneqq \sum_{u=0}^{N-1}\beta(z;(j,0)\to(i,u))e(-\ell u/N) \tag{11}$$

where we introduce the complex exponent notation

$$e(x) = e^{2\pi i x} = \cos(2\pi x) + i\sin(2\pi x) \tag{12}$$

for $x \in \mathbb{R}$. Note that $\hat{\beta}$ is the transform of β in only one azimuthal variable due to the symmetries of β; see (8). The use of the complex Fourier transform here simplifies much of the to-and-fro found in the sign-cosign decomposition. All the while the oscillating properties of the transform may be projected via Euler's identity $e(x) = \cos(x)+i\sin(x)$ or making a simple observation of the real-values of the original functions; see Appendix B.3 for example. We analyse such properties in detail in Appendix B.

Applying the transforms of (10) and (11), for $\mu \in [-1, 1]$ and $z > 0$ we have a *decoupled* spectral RTE for each Fourier-transform index $0 \leq \ell \leq N-1$ given by

$$\tilde{\mu}_i \frac{d}{dz}\hat{L}(z; i; \ell) = -c(z)\hat{L}(z; i; \ell) + \sum_{j=\pm 1}^{M} \hat{\beta}(z; i, j; \ell)\hat{L}(z; j; \ell) + \hat{\sigma}(z; i; \ell). \tag{13}$$

Remark 3.1. The advantage of using the spectral RTE in (13) over the original RTE in (1) is that the ϕ'-integral in (1) is eliminated, or rather 'decoupled' from the dependence on ϕ. The upshot being that the equations indexed by $0 \leq \ell \leq N-1$ may be efficiently solved, independently of one another.

3.4. The discrete spectral RTE as a linear system

To recognise the symmetry in our choice of intervals $\mathcal{I}_i$ and the scattering matrix symmetries (see (8)), we apply $\pm$ index to our notation and henceforth consider $1 \leq i, j \leq M$ by introducing

$$\hat{L}^{\pm}(z; i; \ell) := \hat{L}(z; \pm i; \ell); \quad \hat{\sigma}^{\pm}(z; i; \ell) := \hat{\sigma}(z; \pm i; \ell); \tag{14}$$

and

$$\hat{\beta}^{\pm}(z; i, j; \ell) := \hat{\beta}(z; i, \pm j; \ell) = \hat{\beta}(z; -i, \mp j; \ell). \tag{15}$$

With these conventions, (13) reads as follows:

$$\begin{aligned} \pm \tilde{\mu}_i \frac{d}{dz}\hat{L}^{\pm}(z; i; \ell) = &-c(z)\hat{L}^{\pm}(z; i; \ell) \\ &+ \sum_{j=1}^{M} \left(\hat{\beta}^{\pm}(z; i, j; \ell)\hat{L}^{+}(z; j; \ell) + \hat{\beta}^{\mp}(z; i, j; \ell)\hat{L}^{-}(z; j; \ell) \right) + \hat{\sigma}^{\pm}(z; i; \ell). \end{aligned} \tag{16}$$

Note that (16) is a linear system of M equations. In this vein, we further introduce the following vector notation. For each $\ell = 0, \ldots, N-1$, define the $M \times 1$ column vectors consisting of the M transformed radiance and source terms

$$\hat{L}^{\pm}(z; \ell) := [\hat{L}^{\pm}(z; i; \ell)]_{1 \leq i \leq M}, \ \hat{\sigma}^{\pm}(z; \ell) := [\hat{\sigma}^{\pm}(z; i; \ell)]_{1 \leq i \leq M}.$$

Also define the $M \times M$ 'local transfer matrices' by *the local transmittance matrices*

$$\tau(z; \ell) := \left[\frac{\hat{\beta}^{+}(z; i, j; \ell) - c(z)\delta_{i,j}}{\tilde{\mu}_i} \right]_{1 \leq i, j \leq M}$$

and the *local reflectance matrices*

$$\rho(z; \ell) := \left[\frac{\hat{\beta}^{-}(z; i, j; \ell)}{\tilde{\mu}_i} \right]_{1 \leq i, j \leq M}.$$

These are so-called due to their contribution to preserving the radiance distribution in a given hemisphere: radiation scattered by the matrix $\hat{\beta}^{+}$ remains in the same hemisphere, adjusting its direction within that hemisphere according to τ; on the other hand, radiation scattered by $\hat{\beta}^{-}$ makes a U-turn and is reflected into the opposite hemisphere via ρ. Altogether, Eq. (16) may now be succinctly written as

$$\pm \frac{d}{dz}\hat{L}^{\pm}(z; \ell) = \tau(z; \ell)\hat{L}^{\pm}(z; \ell) + \rho(z; \ell)\hat{L}^{\mp}(z; \ell) + \hat{\sigma}^{\pm}(z; \ell). \tag{17}$$

Condensing notation a final time we henceforth suppress the ℓ-dependence and define the (complete) 2×1 columns of $M \times 1$ vectors

$$\hat{L}(z;\ell) := \begin{bmatrix} \hat{L}^+(z;\ell) \\ \hat{L}^-(z;\ell) \end{bmatrix}, \quad \hat{\sigma}(z;\ell) := \begin{bmatrix} \hat{\sigma}^+(z;\ell) \\ \hat{\sigma}^-(z;\ell) \end{bmatrix}$$

alongside the *local transfer matrix*, the 2×2 array of $M \times M$ matrices

$$K(z;\ell) := \begin{bmatrix} \tau(z;\ell) & \rho(z;\ell) \\ -\rho(z;\ell) & -\tau(z;\ell) \end{bmatrix}. \tag{18}$$

We finally pose the discrete spectral RTE as a $2M$-dimensional system of (in general) non-linear equations

$$\frac{d}{dz}\hat{L}(z;\ell) = K(z;\ell)\hat{L}(z;\ell) + \hat{\sigma}(z;\ell). \tag{19}$$

4. Solving the RTE for bird's-eye views

In this section, we describe the solution implemented in `bird5eye` to generate two-dimensional views over the surface. The conclusion of Section 3 was to neatly package the theoretical components of the original RTE (1) into a linear system of ODEs (19). At face value, in a one dimensional column, this system has two boundary conditions: one at the surface and one at the bottom. To compose our `birdseye` model, we consider a large collection of such columns, each with their own two boundary conditions; a very expensive computational problem for typical solution methods, such as Monte Carlo sampling.

The method of invariant imbedding can solve this system (19) by applying a linear interaction principal across each infinitesimal boundary; see (E.1). Applying this principal to (19) forces a system of ODEs–the Riccati equations given in Appendices E.2 and E.2.2–onto the coefficients of the auxiliary linear relation (E.1). These equations are independent of the original boundary conditions which may be applied post computation, and at any depth. Moreover, the Riccati equations are forward-facing Initial Value Problems (IVPs), thus reducing the original two-point boundary value problem to an easily solved system of IVPs.

In this section we proceed by describing a recipe to assemble this theoretical tool to solve for bird's-eye view projections over a surface area. We exclude the technical details of the invariant imbedding method here, but include them in full in Appendix E.

4.1. Stratified depths over a pixelated area

We describe the water's surface as a collection of pixel coordinates $P = (x, y)$ over a rectangular region $1 \leq x \leq X$ and $1 \leq y \leq Y$. We shall describe a flat surface, so the surface boundary is identical for each P. The procedure below is straightforwardly adapted to describe rough surfaces.

Under the water, we partition the depth-columns underneath each pixel into the following subintervals. Over the pixel $P = (x, y)$, fix an arbitrarily small real number $\varepsilon > 0$ and two indicators of the depth below the pixel P: the 'effective' bottom $b_P > 0$ such that $\mathrm{Chl}(z)$ is constant for $z \geq b_P$; and the 'actual' bottom b'_P. In practice, waters are either considered to have $b'_P = b_P$ or $b'_P \to \infty$, with the latter employed for computational economy where needed. For an arbitrary depth $z \in (\varepsilon, b_P)$ consider the following partition,

$$[-\varepsilon, b'_P] = [-\varepsilon, \varepsilon] \cup [\varepsilon, z] \cup [z, b_P] \cup [b_P, b'_P]. \tag{20}$$

This decomposition describes the complete region of radiative transfer from just above the air–water interface $-\varepsilon$ down to the bottom of the water body b'_P below P. We consider the sky radiance $\hat{L}^+(-\varepsilon)$ incident on (20) as given; see Appendix C.1. Our goal is to determine the water-leaving radiance $\hat{L}^-_P(-\varepsilon)$ above each pixel P. Amending the method below, mutatis mutandis, one obtains the internal radiances $\hat{L}^\pm_P(z)$ for any z, as implemented in `bird5eye`.

By the virtue of the invariant imbedding solution, it suffices to consider only the unique depths b_P, regardless of boundary condition. We henceforth index $b_d = b_P$ for $d = 1, \ldots, D$ recognising that the map $P \mapsto d = d_P$ is many to one. This is possible as we first solve the RTE within the bulk of the water body and append boundary conditions later, as required. Numerically, this reduces the computation by a factor of XY/D.

4.2. Algorithm for radiance computation

The following algorithm shows how to compute the water-leaving radiances $\hat{L}_P^-(-\varepsilon;\ell)$ above each pixel P, with depth-index $d = d_P$. We refer to various formulae detailed in the appendices, starting with the surface boundary condition (C.17) which expresses $\hat{L}_P^-(-\varepsilon;\ell)$ in terms of the unknown radiance $\hat{L}_P^-(\varepsilon;\ell)$. We proceed by solving for this unknown variable.

4.2.1. Step one: In the bulk

Integrate the Riccati equations of Appendix E.2.1 in the bulk from $z = \varepsilon$ to $z = b_d$, thus producing solutions for $T(\varepsilon, b_d)$, $R(b_d, \varepsilon)$, $\Sigma(\varepsilon, b_d)$, $R(\varepsilon, b_d)$, $T(b_d, \varepsilon)$ and $\Sigma(b_d, \varepsilon)$. From the interaction principle (E.1) with $(z_0, z_1) = (\varepsilon, b_d)$ we then have

$$\hat{L}^-(\varepsilon;\ell) = \hat{R}(\varepsilon, b_d;\ell)\hat{L}^+(\varepsilon;\ell) + \hat{T}(b_d, \varepsilon;\ell)\hat{L}^-(b_d;\ell) + \Sigma(b_d, \varepsilon) \tag{21}$$

and

$$\hat{L}^+(b_d;\ell) = \hat{T}(\varepsilon, b_d;\ell)\hat{L}^+(\varepsilon;\ell) + \hat{R}(b_d, \varepsilon;\ell)\hat{L}^-(b_d;\ell) + \Sigma(\varepsilon, b_d). \tag{22}$$

The unknowns in (21) and (22) are $\hat{L}^+(\varepsilon;\ell)$ and $\hat{L}^-(b_d;\ell)$. At this step, the solution depends only on the depth index $d = d_P$.

4.2.2. Step two: Bottom reflections

First of all we extend to the union of intervals $(\varepsilon, b_d)\cup(b_d, b'_d)$. Applying boundary conditions can vary amongst pixels, for example when modelling different colours at each P; we thus append the pixel P to dependent quantities. Following the argument of Appendix E.3 with $(z_0, z_1, z_2) = (\varepsilon, b_d, b'_d)$ we obtain the following transitivity relation for (21):

$$\hat{L}_P^+(b_d;\ell) = (1 - R(b_d, \varepsilon;\ell)R_P(b_d, b'_d;\ell))^{-1}(T(\varepsilon, b_d;\ell)\hat{L}^+(\varepsilon;\ell) + \Sigma_P(\varepsilon, b_d;\ell)); \tag{23}$$

see (E.9) with the substitution of (C.23), noting $\hat{L}^-(b'_d;\ell) = 0$ and $\Sigma(b'_d, b_d;\ell) = 0$ in (b_d, b'_d) by assumption. Together with (C.23) and (23), we rewrite (21) as

$$\hat{L}_P^-(\varepsilon;\ell) = R_P(\varepsilon, b'_d;\ell)\hat{L}^+(\varepsilon;\ell) + \Sigma(b'_d, \varepsilon;\ell). \tag{24}$$

in which

$$\begin{aligned} R_P(\varepsilon, b'_d;\ell) = {} & R(\varepsilon, b_d;\ell) \\ & + T(b_d, \varepsilon;\ell)(1 - R_P(b_d, b'_d;\ell)R(b_d, \varepsilon;\ell))^{-1}R_P(b_d, b'_d;\ell)T(\varepsilon, b_d;\ell) \end{aligned} \tag{25}$$

and

$$\begin{aligned} \Sigma_P(b'_d, \varepsilon;\ell) = {} & T(b_d, \varepsilon;\ell)(1 - R_P(b_d, b'_d;\ell)R(b_d, \varepsilon;\ell))^{-1}R_P(b_d, b'_d;\ell)\Sigma(\varepsilon, b_d;\ell) \\ & + \Sigma(b_d, \varepsilon;\ell). \end{aligned} \tag{26}$$

This is the interaction principle for the interval (ε, b'_d). The assumption that $\hat{L}^-(b'_d;\ell) = 0$ manifests as an absence of transmission $T(b'_d, \varepsilon;\ell)$. In this section, the outputs all depend on specific pixels P (not just the depth $d = d_P$). This is due to the application of pixel-specific bottom reflectances $R_P(b_d, b'_d;\ell)$.

4.2.3. Step three: Through the surface

We lastly append the surface boundary conditions (C.17) to (24). This constitutes applying the transitivity relations of Appendix E.3 with the substitution $(z_0, z_1, z_2) = (-\varepsilon, \varepsilon, b'_d)$ to give

$$\begin{aligned} \hat{L}_P^-(\varepsilon;\ell) = {} & (1 - R_P(\varepsilon, b'_d;\ell)R(\varepsilon, -\varepsilon;\ell))^{-1} \\ & \times (R_P(\varepsilon, b'_d;\ell)T(-\varepsilon, \varepsilon;\ell)\hat{L}^+(-\varepsilon;\ell) + \Sigma_P(b'_d, \varepsilon;\ell)); \end{aligned} \tag{27}$$

see (E.10). With (C.17) to hand, we have an expression for $\hat{L}_P^-(-\varepsilon;\ell)$ in terms of $\hat{L}^+(-\varepsilon;\ell)$, which is assumed given by Appendix C.1. Altogether, we derive the solution for the response radiance on $[-\varepsilon, b'_d] = [-\varepsilon, \varepsilon]\cup[\varepsilon, b_d]\cup[b_d, b'_d]$ by

$$\hat{L}_P^-(-\varepsilon;\ell) = R_P(-\varepsilon, b'_d;\ell)\hat{L}^+(-\varepsilon;\ell) + \Sigma_P(b'_d, -\varepsilon;\ell) \tag{28}$$

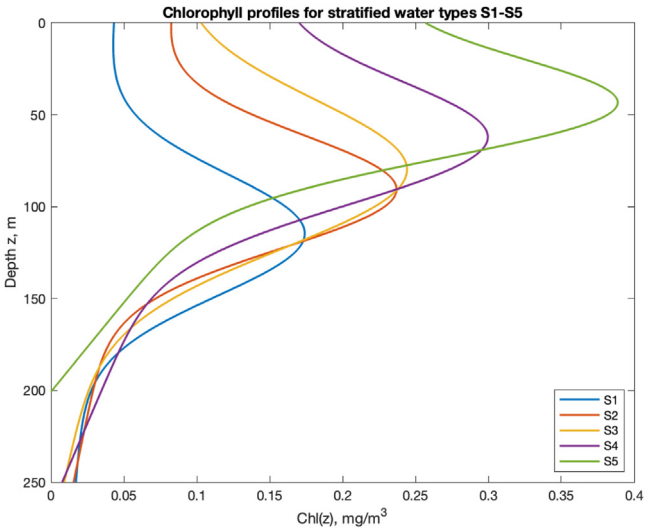

Fig. 4. Deep chlorophyll profile categorise as proposed by [36].

in which

$$R_P(-\varepsilon, b'_d; \ell) = R(-\varepsilon, \varepsilon; \ell) + T(\varepsilon, -\varepsilon; \ell)(1 - R_P(\varepsilon, b'_d; \ell)R(\varepsilon, -\varepsilon; \ell))^{-1} R_P(\varepsilon, b'_d; \ell)T(-\varepsilon, \varepsilon; \ell) \tag{29}$$

and

$$\Sigma(b', -\varepsilon; \ell) = T(-\varepsilon, \varepsilon; \ell)(1 - R_P(\varepsilon, b'_d; \ell)R(\varepsilon, -\varepsilon; \ell))^{-1} \Sigma_P(b'_d, \varepsilon; \ell). \tag{30}$$

To utilise this final equation, apply the embedded definitions of $R_P(\varepsilon, b'_d; \ell)$ in (25) and $\Sigma_P(b'_d, \varepsilon; \ell)$ in (26) alongside the results of Section 4.2.1.

5. Chlorophyll model parameterisation

In this section, we introduce a new approach of ocean categorisation by chlorophyll type [36]. We propose this method as advantageous in contrast to attempts to understand natural waters under Jerlov's classification [17]. A recent approach to apply a Jerlov parameterisation to radiative transfer models was considered by [34]. Typical colour variation using this chlorophyll model is depicted in Fig. 2.

5.1. Gaussian chlorophyll profiles

It is well understood that Chlorophyll profiles of stratified waters may be modelled by Gaussian distributions [20]; see Fig. 4. The depth profile of stratified waters has been classified into nine classes S1–S9 based on a global observation project [36]. This classification has already proved applicable in the field of underwater optical communications [19] and we propose to use this classification here.

The depth profile of chlorophyll concentration Chl(z) mg/m^3 is described by

$$\text{Chl}(z) = A - Bz + C\frac{1}{\sigma\sqrt{2\pi}} \exp\left(-\frac{(z - z_{\max})^2}{2\sigma^2}\right) \tag{31}$$

where the parameters A, B, C; standard deviation σ; and location of the deep chlorophyll maximum (DCM), $z_{\max}$, are derived from the dimensionless quantities considered by [36], recalculated in our framework here in Fig. 5; see Fig. 4 for graphical representation.

Chl. Type / Jerlov Type	A	B	C	σ	$z_{\max}$	Chl($z_{\max}$)
S1 / IA, IB	0.0429	1.03e-4	11.87	33.10	115.41	0.174
S2 / II	0.0805	2.60e-4	13.89	30.73	92.01	0.237
S3 / –	0.0792	2.81e-4	19.08	40.54	82.36	0.244
S4 / III	0.143	5.39e-4	15.95	33.23	65.28	0.299
S5 / –	0.207	10.29e-4	15.35	26.79	46.61	0.387
S6 / –	0.160	7.05e-4	24.72	30.53	33.03	0.460
S7 / 1C	0.329	19.44e-4	25.21	28.62	24.59	0.632
S8 / 3C	1.01	90.30e-4	20.31	17.59	20.38	1.284
S9 / 5C	0.555	0	130.60	20.00	9.87	3.165
CS / –	0.20	0	144	9	17	6.583
NES / –	0.13	0	18	17	72	0.552

Fig. 5. Chlorophyll profile parameters associated to the categories proposed by [36]. Additionally, Celtic Sea (CS) and New England Seamounts are based on measurements made by [31] in May and June, respectively.

6. Experimental

We conducted a submersion experiment using a hyper-spectral camera of a common colour identification chart known as a 'Macbeth' chart; see Fig. 6. This was undertaken at the open tank acoustic characterisation facility at QinetiQ FRN, Fig. 6. Reference was taken above the water's surface (see the top left image in Fig. 7) and used to normalise the model's input sky radiance, as well as the colour conversion. Images were collected every 25 cm between 0–3.5 m. We plot the results at 0, 1, 2, 3 m of the real-life images vs. predictions made with `bird5eye`.

The results observed exhibit the close approximation made by the `bird5eye` model in synthesising submerged colour variation, even in an environment which is difficult to control with respect to a great deal of unknown physical factors (precise water type, optical properties of the tank's surface, possible reflections off the surface of the checker, etc.). Further experimentation into the nature of colour transmission in chlorophyll waters is the intended subject of ongoing research.

Acknowledgments

This work was supported by the U.K. Engineering and Physical Sciences Research Council under grant number EP/R004781/1 (EPSRC and QinetiQ Ltd. through the TEAM-A prosperity partnership, IRH).

Appendix A. Quad averaging functions on the unit ball

A.1. Spherical coordinates

The possible directions into which radiation may be emitted are contained in the unit sphere $\mathcal{B}$. We parameterise $\mathcal{B}$ by the coordinates

$$\mathcal{B} = \{(\mu, \phi) \,|\, \mu \in [-1, 1],\ \phi \in [0, 2\pi)\}$$

where μ is the *polar* coordinate, the projection of the direction onto the z-axis, and ϕ is the *azimuth* which rotates clockwise in a plane parallel to the surface when looking in the positive z-direction and is fixed such that $\phi = 0$ points along $\boldsymbol{x}$, north; see Fig. 3. Explicitly, an arbitrary direction in $\mathcal{B}$ centred at $(0, 0, 0)$ is given by the unit vector

$$\boldsymbol{r} = \boldsymbol{r}(\mu, \phi) := \sin(\arccos(\mu))\cos(\phi)\boldsymbol{x} + \sin(\arccos\mu)\sin(\phi)\boldsymbol{y} + \mu z. \tag{A.1}$$

We further partition $\mathcal{B} = \mathcal{B}^+ \sqcup \mathcal{B}^- \sqcup \mathcal{E}$ into the upper and lower-hemispheres

$$\mathcal{B}^{\pm} := \{(\mu, \phi) \in \mathcal{B} \,:\, \operatorname{sgn}(\mu) = \pm 1\}$$

and the equator $\mathcal{E} := \{(0, \phi) \in \mathcal{B}\}$.

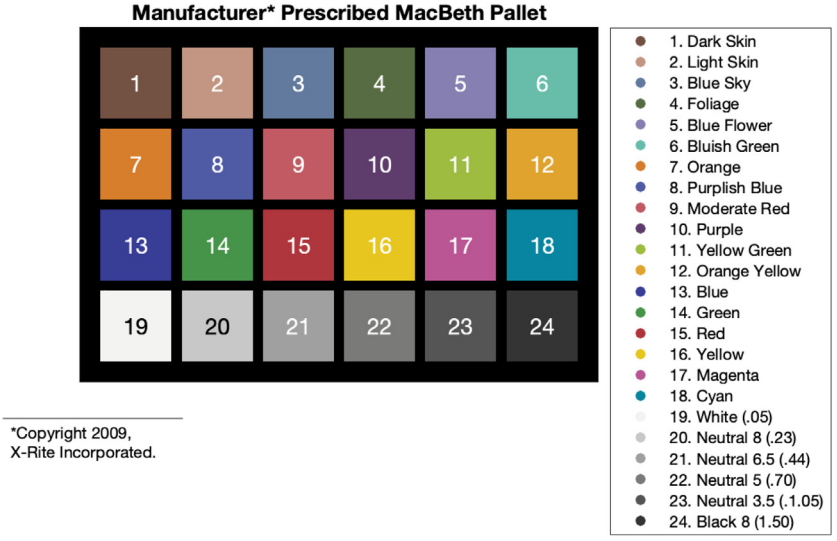

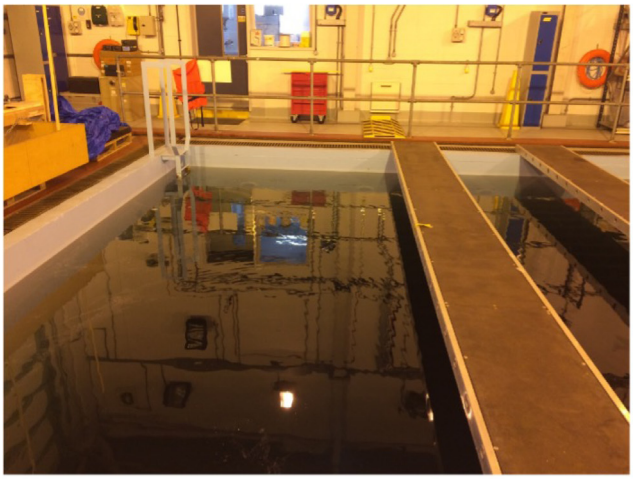

Fig. 6. Macbeth colour checker (top) and experimental water tank (bottom).

A.2. Partitioning the unit sphere

Here we set out explicitly the formulation of the quads described in Section 3.2. We refer to [23, §4.7] but note that our conventions have a different structure.

A.2.1. Polar partition

Fix a positive integer M. We shall divide the polar coordinate μ into $2M$ intervals of equal $\theta := \arccos(\mu)$. Starting at the equator, $\theta = \pi/2$, for $i = 1, \ldots, M$ define M polar angles $\pi/2 > \theta_1 > \cdots > \theta_M > 0$ by

$$\theta_i := \frac{\pi}{2}\left(\frac{M - i + 1/2}{M}\right).$$

Note that if $i \leq M - 1$ then $\theta_{i+1} - \theta_i = \pi/2M$. We then define M polar coordinates in the hemisphere $\mathcal{B}^+$ by

$$\mu_i := \cos(\theta_i).$$

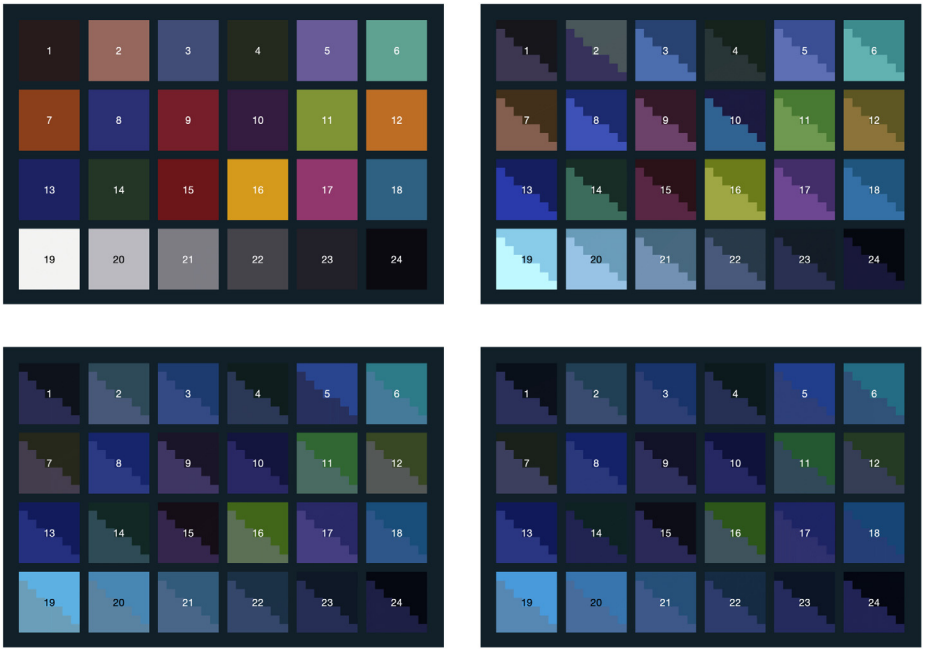

Fig. 7. Experiment depicting `bird5eye` runs (top-right triangle) vs. experimental images (bottom-left) at depths of 0, 1, 2 and 3 m reading left-to-right, top-to-bottom.

We shall consider these as representatives of the intervals

$$\mathcal{I}_i := \left[\cos\left(\frac{\pi}{2}\left(\frac{M-(i-1)}{M}\right)\right), \cos\left(\frac{\pi}{2}\left(\frac{M-i}{M}\right)\right)\right].$$

We denote the length of the intervals by $\Delta\mu_i := \int_{\mathcal{I}_i} d\mu$. This partitions the polar axis of $\mathcal{B}^+$ into intervals of varied length $\Delta\mu_i$. We similarly define $\mu_{-i} := -\mu_i$ determining a representative set of points of $\mathcal{B}^-$ by reflection about 0. The intervals $\mathcal{I}_{-i} := -\mathcal{I}_i$ have length $\Delta\mu_{-i} = \Delta\mu_i$. We shall also require the definition of the average of the end points of $\mathcal{I}_i$ given by

$$\tilde{\mu}_i := \frac{\cos\left(\frac{\pi}{2}\left(\frac{M-i+1}{M}\right)\right) + \cos\left(\frac{\pi}{2}\left(\frac{M-i}{M}\right)\right)}{2}$$

A.2.2. Azimuthal partition

Fix a positive integer N. We firstly approximate the circles defined by $\phi \mapsto \mathbf{r}(\mu, \phi)$ for each $-1 \leq \mu \leq 1$ by an N-gon, reducing analysis on the torus $\mathbb{R}/2\pi\mathbb{Z}$ to that on the finite additive cyclic group $\mathbb{Z}/N\mathbb{Z}$. Define N equally spaced azimuthal coordinates by

$$\phi_u := \frac{2\pi u}{N}$$

for $u = 0, \ldots, N-1$. These points sit centrally in the intervals

$$\mathcal{U}_u := [\phi_u - \tfrac{\pi}{N}, \phi_u + \tfrac{\pi}{N}),$$

determining the partition $[0, 2\pi) = \bigsqcup_{u=0}^{N-1} \mathcal{U}_u$. The length of each $\mathcal{U}_u$ is equal to $2\pi/N$. Identifying the set $[0, 2\pi)$ with $\mathbb{R}/2\pi\mathbb{Z}$, the map $u \mapsto \phi_u$ gives an embedding $\mathbb{Z}/N\mathbb{Z} \hookrightarrow \mathbb{R}/2\pi\mathbb{Z}$. We proceed by only considering functions which pull back uniquely to this finite group.

A.2.3. Solid angle volumes

A solid angle Ω is defined by the area A covered on a sphere as a proportion of the square radius r^2; that is, $\Omega = A/r^2$. This is analogous to the arc-length L of a circular segment of radius r being equal to L/r. An

infinitesimal measure in our spherical coordinate system is then given by

$$d\Omega = d\mu d\phi = \sin(\theta) d\theta d\phi. \tag{A.2}$$

Then, the area of the unit sphere, or otherwise the number of solid radians it contains, is seen to be $\int_0^{2\pi} \int_{-1}^{1} d\mu d\phi = 4\pi$. Our 'quads' over which we discretise the RTE (1) are defined by

$$\mathcal{Q}_{iu} \coloneqq \mathcal{I}_i \times \mathcal{U}_u. \tag{A.3}$$

The solid radian volume of such a quad is then

$$\Delta\mathcal{Q}_{iu} \coloneqq \int_{\mathcal{Q}_{iu}} d\mu d\phi = \frac{2\pi}{N} \Delta\mu_i. \tag{A.4}$$

A.3. Quad averaging functions on the unit sphere

Consider a function $F : \mathcal{B} \to \mathbb{C}$. We consider its average over the quad index by $(\pm i, u)$ to be

$$F(i, u) \coloneqq \frac{1}{\Delta\mathcal{Q}_{iu}} \int_{\mathcal{Q}_{iu}} F(\mu, \phi) d\mu d\phi. \tag{A.5}$$

Similarly, for functions on double quads $G((\mu', \phi') \to (\mu, \phi))$ we define the normalised average

$$G((j, v) \to (i, u)) \coloneqq \frac{1}{\Delta\mathcal{Q}_{iu}} \int_{\mathcal{Q}_{iu}} \int_{\mathcal{Q}_{jv}} G((\mu', \phi') \to (\mu, \phi)) d\mu' d\phi' d\mu d\phi. \tag{A.6}$$

We refer to [23, §4.7] for a wider description of the properties of these functions.

A.4. Quad averaged irradiance

The up $E^-(z)$ or downward $E^+(z)$ pointing irradiance from a flat surface is related to the radiance via

$$E^{\pm}(z) = \int_{\mathcal{B}^{\pm}} L(z; \mu, \phi) \mu d\mu d\phi. \tag{A.7}$$

To compute the irradiance from quad averaged radiance values $L(z; i, v)$ we simply observe that

$$E^{\pm}(z) = \sum_{i=0}^{M} \sum_{u=0}^{N} L^{\pm}(z; i, u) \tilde{\mu}_i \Delta\mathcal{Q}_{iu}. \tag{A.8}$$

Appendix B. Complex Fourier transforms and the spectral RTE

Here we derive the formula given in (13) which asks for analysis of the complex Fourier transform. We contrast this derivation with the extended derivation in [23] for the real-Fourier transform. Using complex coefficients permits the use of in-built parallel programming for complex number computations. Meanwhile, the tangible coefficient information is compactly packaged and readily accessible when specifying that the original function is real valued; see Appendix B.3 for example.

B.1. Fourier inversion on a finite group

A periodic function $f : \mathbb{R}/2\pi\mathbb{Z} \to \mathbb{C}$ is naturally restricted to a function $\mathbb{Z}/N\mathbb{Z} \to \mathbb{C}$ via $u \mapsto f(\phi_u)$. For each integer $0 \leq \ell \leq N - 1$, we thus define the *finite Fourier transform* of f by

$$\hat{f}(\ell) \coloneqq \sum_{u=0}^{N-1} f(\phi_u) e(-\ell u / N), \tag{B.1}$$

recalling that $e(x) = e^{2\pi i x}$ for $x \in \mathbb{R}$. For $0 \leq u \leq N - 1$, the orthogonality relation

$$\frac{1}{N} \sum_{\ell=0}^{N-1} e((\ell - u)/N) = \delta_{u,0} \tag{B.2}$$

implies the inversion formula

$$f(\phi_u) = \frac{1}{N}\sum_{\ell=0}^{N-1} \hat{f}(\ell) e(\ell u/N). \tag{B.3}$$

If $f(x) \in \mathbb{R}$ for each $x \in \mathbb{R}$, we use the Euler's identity, $e(x) = \cos(x) + i\sin(x)$, to evaluate the real part of (B.1) so that the expansion (B.3) is expressed in terms of trigonometric functions.

B.2. Transforming the spectral RTE

We apply the procedure given in Appendix B.1 to the discrete RTE (9) by introducing the transforms in (10) and (11). Substituting these into (9) via the inversion formula (B.3) and applying (8) to evaluate the ϕ'-integral as a summation, we obtain

$$\begin{aligned}\tilde{\mu}_i \frac{d}{dz}\sum_{\ell=0}^{N-1} \hat{L}(z;i;\ell)e(\ell u/N) = &-c(z)\sum_{\ell=0}^{N-1}\hat{L}(z;i;\ell)e(\ell u/N)\\ &+\frac{1}{N}\sum_{v=0}^{N-1}\sum_{j=\pm 1}^{\pm M}\sum_{\ell=0}^{N-1}\hat{\beta}(z;i,j;\ell)e(\ell(u-v)/N)\sum_{k=0}^{N-1}\hat{L}(z;j;k)e(kv/N)\\ &+\sum_{\ell=0}^{N-1}\hat{\sigma}(z;\mu;\ell)e(\ell u/N).\end{aligned} \tag{B.4}$$

Reordering the (v,ℓ,k) summations as (ℓ,k,v) and evaluating the orthogonal v-sum per (B.2), Eq. (B.4) simplifies to

$$\begin{aligned}\tilde{\mu}_i \sum_{\ell=0}^{N-1} e(\ell u/N)\frac{d}{dz}\hat{L}(z;i;\ell) = &-c(z)\sum_{\ell=0}^{N-1} e(\ell u/N)\hat{L}(z;i;\ell)\\ &+\sum_{\ell=0}^{N-1} e(\ell u/N)\left(\sum_{j=\pm 1}^{\pm M}\hat{\beta}(z;i,j;\ell)\hat{L}(z;j;\ell)d\mu' + \hat{\sigma}(z;i;\ell)\right).\end{aligned} \tag{B.5}$$

Lemma B.1 (*Equating ℓ-Coefficients*). *For each $u = 0,\dots,1-N$ suppose that $c_\ell \in \mathbb{C}$ satisfies $\sum_{\ell=0}^{N-1} e(\ell u/N)c_\ell = 0$. Then $c_\ell = 0$ for all $\ell = 0,\dots,N-1$.*

Proof. Consider the $N\times N$ matrix $A := (e((i-1)(j-1)/N))_{1\le i,j\le N}$ and $N\times 1$ column vector $C := (c_{j-1})_{1\le j\le N}$. By the hypothesis we have that $AC = 0_{N\times 1}$. Moreover, the Vandermonde matrix A is invertible, with inverse A^{-1}, as is seen by evaluating the determinant

$$\det(A) = \prod_{1\le i<j\le N}(e(j-1) - e(i-1)) \neq 0.$$

The lemma now follows from the equality $C = A^{-1}0_{N\times 1} = 0_{N\times 1}$. □

By Lemma B.1 this assertion, the ℓ-summands in (B.5) now decouple as follows.

B.3. Coefficient elimination for real-valued functions

Let N be even. For a real valued function $f(u)$ on $\mathbb{Z}/N\mathbb{Z}$ with finite Fourier transform $\hat{f}(\ell) = \sum_{u=0}^{N-1} f(u)\, e(-u\ell/N)$ we take the complex conjugate $z^* = x - iy$ to deduce,

$$\hat{f}(\ell)^* = \sum_{u=0}^{N-1} f(u)e(u\ell/N) = \hat{f}(-\ell) = \hat{f}(N-\ell). \tag{B.6}$$

Applying the Fourier inversion formula we deduce

$$f(u) = \frac{1}{N}\sum_{\ell=0}^{\frac{N}{2}-1} \hat{f}(\ell)e(u\ell/N) + \frac{1}{N}\sum_{\ell=\frac{N}{2}}^{N-1} \hat{f}(\ell)e(u\ell/N)$$
$$= \frac{1}{N}\sum_{\ell=0}^{\frac{N}{2}-1} \left[\hat{f}(\ell)e(u\ell/N) + \hat{f}(\ell+1)^* e(-u(\ell+1)/N)\right] \tag{B.7}$$

which only requires the evaluation of $\hat{f}(\ell)$ for $\ell = 0, \ldots, N/2$.

Appendix C. Boundary conditions

C.1. Sky radiance sources

Light incident on the water's surface is an input to the surface boundary condition and so must be assigned. For recreational purposes this can be set arbitrarily as it does not affect irradiance reflectance computations. For our experiments in Section 6 we insert the measured value. For real-world data we collect two sources (implemented in `bird5eye`): spectral data recorded by Chance–Kurucz [7] gives the solar irradiance onto the earth's surface, this may be obtained from www.nrel.gov/grid/solar-resource/spectra.html; an atmospheric propagation model is provided by [16], based on [29], to give sensitivity to factors such as could coverage and low visibility. We also implement a geolocation-based solar angle model to give the solar zenith with respect to a given date-time.

C.2. The surface boundary

At the surface, we consider approaching the air–water interface from each side separately. This is achieved by considering an arbitrarily small real number $\varepsilon > 0$ and assessing the distribution of radiance at both $\varepsilon\mathbf{z}$ and $-\varepsilon\mathbf{z}$. We require the reflection and transmission functions as light travels over this interface $[-\varepsilon, \varepsilon]$. For an incident beam in direction $\boldsymbol{r}' \in \mathcal{B}^{\pm}$, denote the ratio reflected into direction $\boldsymbol{r} \in \mathcal{B}^{\mp}$ at $\mp\varepsilon$ by $R(\mp\varepsilon, \pm\varepsilon; \boldsymbol{r}'\to\boldsymbol{r})$. For an incident beam in direction $\boldsymbol{r}' \in \mathcal{B}^{\pm}$, denote the ratio transmitted into direction $\boldsymbol{r} \in \mathcal{B}^{\pm}$ at $\pm\varepsilon$ by $T(\mp\varepsilon, \pm\varepsilon; \boldsymbol{r}'\to\boldsymbol{r})$. These quantities are prescribed by Snell's law in the transmission of light across the surface boundary. For $\boldsymbol{r} \in \mathcal{B}^{\pm}$, the associated boundary conditions are given by

$$L(\pm\varepsilon; \boldsymbol{r}) = \int_{\mathcal{B}^{\pm}} T(\mp\varepsilon, \pm\varepsilon; \boldsymbol{r}'\to\boldsymbol{r}) d\boldsymbol{r}' L(\mp\varepsilon; \boldsymbol{r}')$$
$$+ \int_{\mathcal{B}^{\mp}} R(\pm\varepsilon, \mp\varepsilon; \boldsymbol{r}'\to\boldsymbol{r}) L(\pm\varepsilon; \boldsymbol{r}') d\boldsymbol{r}'; \tag{C.1}$$

see [23, (4.66) & (4.67)].

C.3. The bottom boundary

We mark the 'effective' bottom, the deepest point to which we solve (1) in general, by $z = b$. The true bottom of the water body shall be denoted by b' and can take one of two forms:

- A diffusely scattering, finite (Lambertian) bottom. In this case, we take $b' = b$.
- An infinitely deep bottom $b' \to \infty$. In this case, we simply choose b large enough so that radiative transfer in the region $[b, \infty)$ is a homogeneous and source free.

In either case, we require the reflectance at b for the region $[b, b']$. For $\boldsymbol{r}' \in \mathcal{B}^{+}$ and $\boldsymbol{r} \in \mathcal{B}^{-}$, this prescribed value is denoted by $R(b, b'; \boldsymbol{r}'\to\boldsymbol{r})$ and (cf. (C.1)) satisfies

$$L(b; \boldsymbol{r}) = \int_{\mathcal{B}^{+}} R(b, b'; \boldsymbol{r}'\to\boldsymbol{r}) L(b; \boldsymbol{r}') d\boldsymbol{r}'. \tag{C.2}$$

If at $b' = b$ the surface is diffusely scattering with irradiance reflectance R then the reflection coefficient is given by

$$R(b, b'; (\mu', \phi') \to (\mu, \phi)) = \frac{R}{\pi}\mu'. \tag{C.3}$$

Indeed, this respects the definition of irradiance reflectance, $R = E^-(b)/E^+(b)$, since

$$E^-(b) = \int_{\mathcal{B}^-}\int_{\mathcal{B}^+} L(b; \mu', \phi')\frac{R}{\pi}\mu' d\mu' d\phi' |\mu| d\mu d\phi \tag{C.4}$$

$$= \frac{R}{\pi}E^+(b)\int_0^{2\pi}\int_0^{-1} \mu' d\mu' d\phi' = R. \tag{C.5}$$

In particular, the radiance at μ, ϕ reflected from a Lambertian surface is given by

$$L(b; \mu, \phi) = \int_{\mathcal{B}^+} L(b; \mu', \phi')\frac{R}{\pi}\mu' d\mu' d\phi' = \frac{R}{\pi}E^-(b) \tag{C.6}$$

for $(\mu, \phi) \in \mathcal{B}^-$.

C.4. Discrete spectral boundary conditions

Analogously, we transform the boundary conditions (C.1) and (C.2), first discretely, in a quad-averaged sense, and then by Fourier decomposition as in Section 3.3 via the azimuthal Fourier transform in Appendix B.

C.4.1. The discrete spectral surface boundary

Firstly, to (C.1) we apply the quad averaging technique over $\mathcal{Q}_{iu}$ to obtain the discrete boundary condition

$$L^\pm(\pm\varepsilon; i, u) = \sum_{v=0}^{N-1}\sum_{j=1}^{M}\Big(T(\mp\varepsilon, \pm\varepsilon; (\pm j, v)\to(\pm i, u))L^\pm(\mp\varepsilon; j, v) + R(\pm\varepsilon, \mp\varepsilon; (\mp j, v)\to(\pm i, u))L^\mp(\pm\varepsilon; j, v)\Big) \tag{C.7}$$

for $1 \le i \le M$ and $0 \le v \le N-1$. We introduce double Fourier transforms, in each variable u, v, given by

$$\hat{R}(\pm\varepsilon, \mp\varepsilon; i, j; \ell, k) := \sum_{u=0}^{N-1}\sum_{v=0}^{N-1} R(\pm\varepsilon, \mp\varepsilon; (\mp j, v)\to(\pm i, u))e(-(\ell u + kv)/N) \tag{C.8}$$

and

$$\hat{T}(\mp\varepsilon, \pm\varepsilon; i, j; \ell, k) := \sum_{u=0}^{N-1}\sum_{v=0}^{N-1} T(\mp\varepsilon, \pm\varepsilon; (\pm j, v)\to(\pm i, u))e(-(\ell u + kv)/N). \tag{C.9}$$

Substituting these alongside (10) and (11) then following the procedure described in Appendix B.2 we derive the discrete spectral surface boundary condition:

$$\hat{L}^\pm(\pm\varepsilon; i; \ell) = \frac{1}{N}\sum_{k=0}^{N-1}\sum_{j=1}^{M}\Big(\hat{T}(\mp\varepsilon, \pm\varepsilon; i, j; \ell, k)\hat{L}^\pm(\mp\varepsilon; j; k) + \hat{R}(\pm\varepsilon, \mp\varepsilon; i, j; \ell, k)\hat{L}^\mp(\pm\varepsilon; j; k)\Big) \tag{C.10}$$

for $1 \le i \le M$ and $0 \le \ell \le N-1$. Defining the matrices

$$\hat{R}(\pm\varepsilon, \mp\varepsilon; \ell, k) := \Big[\hat{R}(\pm\varepsilon, \mp\varepsilon; i, j; \ell, k)\Big]_{1\le i,j\le M} \tag{C.11}$$

and

$$\hat{T}(\mp\varepsilon, \pm\varepsilon; \ell, k) := \Big[\hat{T}(\mp\varepsilon, \pm\varepsilon; i, j; \ell, k)\Big]_{1\le i,j\le M} \tag{C.12}$$

we rewrite (C.10) as

$$\begin{bmatrix} \hat{L}^+(+\varepsilon;\ell) \\ \hat{L}^-(-\varepsilon;\ell) \end{bmatrix} = \frac{1}{N}\sum_{k=0}^{N-1} \begin{bmatrix} \hat{T}(-\varepsilon,+\varepsilon;\ell,k) & \hat{R}(+\varepsilon,-\varepsilon;\ell,k) \\ \hat{R}(-\varepsilon,+\varepsilon;\ell,k) & \hat{T}(+\varepsilon,-\varepsilon;\ell,k) \end{bmatrix} \begin{bmatrix} \hat{L}^+(-\varepsilon;k) \\ \hat{L}^-(+\varepsilon;k) \end{bmatrix} \tag{C.13}$$

for $0 \le \ell \le N-1$.

We extend this formula by devising $MN \times MN$ matrices

$$\hat{R}(\pm\varepsilon,\mp\varepsilon) := \left[\frac{1}{N}\hat{R}(\pm\varepsilon,\mp\varepsilon;\ell,k)\right]_{1\le\ell,k\le N} \tag{C.14}$$

and

$$\hat{T}(\mp\varepsilon,\pm\varepsilon) := \left[\frac{1}{N}\hat{T}(\mp\varepsilon,\pm\varepsilon;\ell,k)\right]_{1\le\ell,k\le N} \tag{C.15}$$

and an MN-length column vector

$$\hat{L}^{\pm}(\pm\varepsilon) := \left[\hat{L}^{\pm}(\pm\varepsilon;\ell)\right]_{1\le\ell\le N} \tag{C.16}$$

so that the boundary condition is expressible as

$$\begin{bmatrix} \hat{L}^+(+\varepsilon) \\ \hat{L}^-(-\varepsilon) \end{bmatrix} = \begin{bmatrix} \hat{T}(-\varepsilon,+\varepsilon) & \hat{R}(+\varepsilon,-\varepsilon) \\ \hat{R}(-\varepsilon,+\varepsilon) & \hat{T}(+\varepsilon,-\varepsilon) \end{bmatrix} \begin{bmatrix} \hat{L}^+(-\varepsilon) \\ \hat{L}^-(+\varepsilon) \end{bmatrix}. \tag{C.17}$$

C.4.2. The discrete spectral bottom boundary

At the bottom, we rewrite (C.2) as the discrete boundary condition

$$L^-(b;i,v) = \sum_{u=0}^{N-1}\sum_{j=1}^{M} R(b,b';(j,u)\to(-i,v))L(b;j,u) \tag{C.18}$$

for $1 \le i \le M$ and $0 \le v \le N-1$. Note that, in both the Lambertian and infinite cases, we assume that, $R(b,b';(j,u)\to(-i,v)) = R(b,b';(j,0)\to(-i,v-u))$ thus simplifying the necessary transform. In the Lambertian case, where the surface is diffusely scattering with irradiance reflectance R then the quad averaged reflection coefficient, defined by (A.6), is given by

$$R(b,b';(j,v)\to(i,u)) = \int_{\mathcal{Q}_{jv}} \frac{R}{\pi}\mu' d\mu' d\phi' = \frac{R}{\pi}\Delta\mathcal{Q}_{jv}\tilde{\mu}_j. \tag{C.19}$$

Introducing the transform,

$$\hat{R}(b;i,j;\ell) := \sum_{v=0}^{N-1} R(b,b';(j,0)\to(-i,v))e(-\ell v/N) \tag{C.20}$$

one derives the discrete spectral bottom boundary condition

$$\hat{L}^-(b;i;\ell) = \sum_{j=1}^{M} \hat{L}(b;j;\ell)\hat{R}(b;i,j;\ell) \tag{C.21}$$

for $1 \le i \le M$ and $0 \le \ell \le N-1$. Similarly, defining

$$\hat{R}(b;\ell) := \left[\hat{R}(b;i,j;\ell)\right]_{1\le i,j\le M} \tag{C.22}$$

we may rewrite (C.21) as

$$\hat{L}^-(b;\ell) = \hat{R}(b;\ell)\hat{L}^+(b;\ell). \tag{C.23}$$

C.5. Collecting spectral identities in matrix form

Note that any such linear identity of the form

$$\begin{bmatrix} \hat{L}^+(z_1;\ell) \\ \hat{L}^-(z_0;\ell) \end{bmatrix} = \begin{bmatrix} \hat{T}(z_0,z_1;\ell) & \hat{R}(z_1,z_0;\ell) \\ \hat{R}(z_0,z_1;\ell) & \hat{T}(z_1,z_0;\ell) \end{bmatrix} \begin{bmatrix} \hat{L}^+(z_0;\ell) \\ \hat{L}^-(z_1;\ell) \end{bmatrix}. \tag{C.24}$$

may be expressed in terms of the vector

$$\hat{L}^{\pm}(z) \coloneqq \left[\hat{L}^{\pm}(z;\ell)\right]_{1\le\ell\le N} \tag{C.25}$$

by introducing the block diagonal matrices

$$\hat{R}(z_a, z_b) \coloneqq \operatorname{diag}\left(\left[\hat{R}(z_a, z_b;\ell)\right]_{1\le\ell\le N}\right) \tag{C.26}$$

and

$$\hat{T}(z_a, z_b) \coloneqq \operatorname{diag}\left(\left[\hat{T}(z_a, z_b;\ell,k)\right]_{1\le\ell,k\le N}\right) \tag{C.27}$$

so that (C.24), for each $0 \le \ell \le N-1$ becomes

$$\begin{bmatrix} \hat{L}^{+}(z_1) \\ \hat{L}^{-}(z_0) \end{bmatrix} = \begin{bmatrix} \hat{T}(z_0, z_1) & \hat{R}(z_1, z_0) \\ \hat{R}(z_0, z_1) & \hat{T}(z_1, z_0) \end{bmatrix} \begin{bmatrix} \hat{L}^{+}(z_0) \\ \hat{L}^{-}(z_1) \end{bmatrix}. \tag{C.28}$$

Appendix D. The fundamental solution

One may in fact write down an explicit solution to (19). Fix two depths $z_1 > z_0 > 0$. We seek an analytic solution $\hat{L}(z)$, the 'state vector', at $z = z_1$ given the initial value $\hat{L}(z_0)$. To this end we introduce a *state-transition matrix* $\Phi(z, z_0) \coloneqq F(z)F(z_0)^{-1}$ where the $M \times M$ matrix $F(z)$ is a 'fundamental solution' to the associated homogeneous problem $\frac{dF}{dz}(z) = K(z)F(z)$. This non-explicit definition directly implies the following properties: $\Phi(z_0, z_0) = 1$; $\Phi(z_1, z_0) = \Phi(z_1, z)\Phi(z, z_0)$ for $z > 0$; $\Phi(z_1, z_0) = \Phi(z_0, z_1)^{-1}$ and

$$\frac{d}{dz_1}\Phi(z_1, z_0) = K(z_1)\Phi(z_1, z_0). \tag{D.1}$$

Using Lagrange's method of variation of parameters, the general solution to (19) is given by

$$\hat{L}(z_1) = \Phi(z_1, z_0)\hat{L}(z_0) + \int_{z_0}^{z_1} \Phi(z_1, z)\hat{\sigma}(z)dz. \tag{D.2}$$

(See [35, §2.4] for expanded details.) Whilst we do not use this solution explicitly, its existence is crucial for the invariant imbedding method, Appendix E.

Appendix E. Invariant imbedding relations

The invariant imbedding relations that we apply to `bird5eye` are derived by considering a solution to (19) in terms of the incident and response radiances on a given interval. We derive these here over an arbitrary interval $[z_0, z_1]$. This solution fuels the general model solution outlined in Section 4. In this section, we amend the notation of (19) by fixing $0 \le \ell \le N-1$ and excluding its mention from the formulae here.

E.1. The linear interaction principle

Fix two depths $z_1 > z_0 > 0$. We consider 'response' radiances $\hat{L}^{+}(z_1)$ and $\hat{L}^{-}(z_0)$ of the interval $[z_0, z_1]$ in terms of the 'incident' radiances $\hat{L}^{+}(z_0)$ and $\hat{L}^{-}(z_1)$ on it. Rearranging the fundamental solution (D.2) to solve for the response radiances we obtain the *linear interaction principle*:

$$\begin{bmatrix} \hat{L}^{+}(z_1) \\ \hat{L}^{-}(z_0) \end{bmatrix} = \begin{bmatrix} T(z_0, z_1) & R(z_1, z_0) \\ R(z_0, z_1) & T(z_1, z_0) \end{bmatrix} \begin{bmatrix} \hat{L}^{+}(z_0) \\ \hat{L}^{-}(z_1) \end{bmatrix} + \begin{bmatrix} \Sigma(z_0, z_1) \\ \Sigma(z_1, z_0) \end{bmatrix}. \tag{E.1}$$

The coefficients R, T and Σ may be derived from (19) and, in particular, all depend on the fixed integer $0 \le \ell \le N-1$. We consider the R terms as locally measuring the reflection of radiance, T the transmission, and Σ the source contribution. Note that the ordering of (z_0, z_1) or (z_1, z_0) indicates the original direction of the incident beam, the former corresponding to $\mathcal{B}^{+}$ and the latter to $\mathcal{B}^{-}$.

Whilst these coefficients may be expressed explicitly, the approach of invariant imbedding is to consider their slight variation over the family of problems as z_0 and z_1 vary.

E.2. The Riccati differential equations

In this section we derive differential equations for the coefficients R, T and Σ that may be solved as initial value problems in order to explicate (E.1). The routine to achieve this is as follows:

1. Fix one of z_0 or z_1 and consider the other as a free variable.
2. Differentiate the interaction principle (E.1) with respect to the free variable.
3. Substitute the expression for the RTE (19) in place of the derivatives of any $\hat{L}^{\pm}$.
4. Substitute any response radiances $\hat{L}^{+}(z_1)$ and $\hat{L}^{-}(z_0)$ with their expressions in (E.1) to result in an expression involving derivatives of the R, T and $\Sigma^{\pm}$ and incident radiances.
5. The resulting equations hold for any choice of incident radiances $\hat{L}^{+}(z_1)$ and $\hat{L}^{-}(z_0)$. We then argue by their linear independence in order to derive identities amongst their coefficients. These are the Riccati differential equations.

E.2.1. Six downward equations

Firstly, we consider z_0 as a fixed constant and $z_1 > z_0$ a free variable. As described above, starting with $\hat{L}^{+}(z_1) = T(z_0, z_1)\hat{L}^{+}(z_0) + R(z_1, z_0)\hat{L}^{-}(z_1) + \Sigma(z_0, z_1)$ we obtain the following:

$$\begin{aligned}
\frac{d}{dz_1}T(z_0, z_1) &= [\tau(z_1) + R(z_1, z_0)\rho(z_1)]\, T(z_0, z_1) \\
\frac{d}{dz_1}R(z_1, z_0) &= [\tau(z_1) + R(z_1, z_0)\rho(z_1)]\, R(z_1, z_0) + R(z_1, z_0)\tau(z_1) + \rho(z_1) \\
\frac{d}{dz_1}\Sigma(z_0, z_1) &= [\tau(z_1) + R(z_1, z_0)\rho(z_1)]\, \Sigma(z_0, z_1) + R(z_1, z_0)\sigma^{-}(z_1) + \sigma^{+}(z_1)
\end{aligned} \tag{E.2}$$

Starting with $\hat{L}^{-}(z_0) = R(z_0, z_1)\hat{L}^{+}(z_0) + T(z_1, z_0)\hat{L}^{-}(z_1) + \Sigma(z_1, z_0)$ we determine the remaining downward equations:

$$\begin{aligned}
\frac{d}{dz_1}R(z_0, z_1) &= T(z_1, z_0)\rho(z_1)T(z_0, z_1) \\
\frac{d}{dz_1}T(z_1, z_0) &= T(z_1, z_0)\,[\tau(z_1) + \rho(z_1)R(z_1, z_0)] \\
\frac{d}{dz_1}\Sigma(z_1, z_0) &= T(z_1, z_0)\left[\rho(z_1)\Sigma(z_0, z_1) + \sigma^{-}(z_1)\right]
\end{aligned} \tag{E.3}$$

Initial conditions for the equations in (E.2) and (E.3) are obtained from (E.1), whence

$$\begin{aligned}
T(z_0, z_0) &= \mathbf{1}_{M\times M} \\
R(z_0, z_0) &= \mathbf{0}_{M\times M} \\
\Sigma(z_0, z_0) &= \mathbf{0}_{M\times 1}.
\end{aligned} \tag{E.4}$$

E.2.2. Six upward equations

Secondly, we consider z_1 as a fixed constant and $z_0 < z_1$ a free variable. Starting with $\hat{L}^{+}(z_1) = T(z_0, z_1)\hat{L}^{+}(z_0) + R(z_1, z_0)\hat{L}^{-}(z_1) + \Sigma(z_0, z_1)$ we obtain the following:

$$\begin{aligned}
-\frac{d}{dz_0}T(z_0, z_1) &= T(z_0, z_1)\,[\tau(z_0) + \rho(z_0)R(z_0, z_1)] \\
-\frac{d}{dz_0}R(z_1, z_0) &= T(z_0, z_1)\rho(z_0)T(z_1, z_0) \\
-\frac{d}{dz_0}\Sigma(z_0, z_1) &= T(z_0, z_1)\left[\rho(z_0)\Sigma(z_1, z_0) + \sigma^{+}(z_0)\right]
\end{aligned} \tag{E.5}$$

Starting with $\hat{L}^-(z_0) = R(z_0, z_1)\hat{L}^+(z_0) + T(z_1, z_0)\hat{L}^-(z_1) + \Sigma(z_1, z_0)$ we determine the remaining downward equations:

$$\begin{aligned}
-\frac{d}{dz_0}R(z_0, z_1) &= [\tau(z_0) + R(z_0, z_1)\rho(z_0)]\, R(z_0, z_1) + R(z_0, z_1)\tau(z_0) + \rho(z_0) \\
-\frac{d}{dz_0}T(z_1, z_0) &= [\tau(z_0) + R(z_0, z_1)\rho(z_0)]\, T(z_1, z_0) \\
-\frac{d}{dz_0}\Sigma(z_1, z_0) &= [\tau(z_0) + R(z_0, z_1)\rho(z_0)]\, \Sigma(z_1, z_0) + R(z_0, z_1)\sigma^+(z_0) + \sigma^-(z_0)
\end{aligned} \tag{E.6}$$

Initial conditions for the equations in (E.5) and (E.6) are obtained from (E.1), whence

$$\begin{aligned}
T(z_1, z_1) &= \mathbf{1}_{M\times M} \\
R(z_1, z_1) &= \mathbf{0}_{M\times M} \\
\Sigma(z_1, z_1) &= \mathbf{0}_{M\times 1}.
\end{aligned} \tag{E.7}$$

E.3. Transitivity relations

Now fix $z_2 > z_1 > z_0$. We consider how the interaction principle (E.1) behaves transitively over the interval

$$[z_0, z_2] = [z_0, z_1] \cup [z_0, z_2].$$

The given incident radiances on $[z_0, z_2]$ are $\hat{L}^+(z_0)$ and $\hat{L}^-(z_2)$ and we consider the system as solved when we may compute the responses $\hat{L}^-(z_0)$ and $\hat{L}^+(z_2)$. We do this by deriving linear interaction principles for the full interval $[z_0, z_2]$. We begin with (E.1) for each of the subintervals $[z_0, z_1]$ and $[z_1, z_2]$:

$$\begin{aligned}
\hat{L}^+(z_2) &= T(z_1, z_2)\hat{L}^+(z_1) + R(z_2, z_1)\hat{L}^-(z_2) + \Sigma(z_1, z_2) \\
\hat{L}^-(z_1) &= R(z_1, z_2)\hat{L}^+(z_1) + T(z_2, z_1)\hat{L}^-(z_2) + \Sigma(z_2, z_1) \\
\hat{L}^+(z_1) &= T(z_0, z_1)\hat{L}^+(z_0) + R(z_1, z_0)\hat{L}^-(z_1) + \Sigma(z_0, z_1) \\
\hat{L}^-(z_0) &= R(z_0, z_1)\hat{L}^+(z_0) + T(z_1, z_0)\hat{L}^-(z_1) + \Sigma(z_1, z_0)
\end{aligned} \tag{E.8}$$

Next, by substitution, we express $\hat{L}^+(z_1)$ and $\hat{L}^-(z_1)$, the intermediate terms, in terms of the incident radiances on $[z_0, z_2]$. We thus derive

$$\hat{L}^+(z_1) = \boldsymbol{T}(z_0, z_1, z_2)\hat{L}^+(z_0) + \boldsymbol{R}(z_2, z_1, z_0)\hat{L}^-(z_2) + \boldsymbol{\Sigma}(z_0, z_1, z_2) \tag{E.9}$$

and

$$\hat{L}^-(z_1) = \boldsymbol{R}(z_0, z_1, z_2)\hat{L}^+(z_0) + \boldsymbol{T}(z_2, z_1, z_0)\hat{L}^-(z_2) + \boldsymbol{\Sigma}(z_2, z_1, z_0) \tag{E.10}$$

where

$$\begin{aligned}
\boldsymbol{T}(z_0, z_1, z_2) &= (1 - R(z_1, z_0)R(z_1, z_2))^{-1}T(z_0, z_1) \\
\boldsymbol{R}(z_2, z_1, z_0) &= (1 - R(z_1, z_0)R(z_1, z_2))^{-1}R(z_1, z_0)T(z_2, z_1) \\
\boldsymbol{\Sigma}(z_0, z_1, z_2) &= (1 - R(z_1, z_0)R(z_1, z_2))^{-1}(R(z_1, z_0)\Sigma(z_2, z_1) + \Sigma(z_0, z_1)) \\
\boldsymbol{R}(z_0, z_1, z_2) &= (1 - R(z_1, z_2)R(z_1, z_0))^{-1}R(z_1, z_2)T(z_0, z_1) \\
\boldsymbol{T}(z_2, z_1, z_0) &= (1 - R(z_1, z_2)R(z_1, z_0))^{-1}T(z_2, z_1) \\
\boldsymbol{\Sigma}(z_2, z_1, z_0) &= (1 - R(z_1, z_2)R(z_1, z_0))^{-1}(R(z_1, z_2)\Sigma(z_0, z_1) + \Sigma(z_2, z_1)).
\end{aligned} \tag{E.11}$$

Remark E.1. We pause this mathematical derivation to observe the physical significance of the terms involved. Recall that we have the following identity for the geometric series,

$$\frac{1}{1-X} = 1 + X + X^2 + X^3 + \cdots$$

valid for $X < 1$. Such terms occur in the above and signify the accruing of multiple reflections across the dissected interval $[z_0, z_2]$. We refer to [23, Fig. 7.1, Ch. 7, p. 351] for a graphical discussion of this phenomenon.

Lastly, inserting (E.9) and (E.10) into the expressions for $\hat{L}^+(z_2)$ and $\hat{L}^-(z_0)$ in (E.8) one obtains global interaction principles for $[z_0, z_2]$:

$$\begin{aligned}\hat{L}^+(z_2) &= T(z_1,z_2)\boldsymbol{T}(z_0,z_1,z_2)\hat{L}^+(z_0)\\ &\quad + (T(z_1,z_2)\boldsymbol{R}(z_2,z_1,z_0) + R(z_2,z_1))\hat{L}^-(z_2)\\ &\quad + T(z_1,z_2)\boldsymbol{\Sigma}(z_0,z_1,z_2) + \Sigma(z_1,z_2).\end{aligned} \tag{E.12}$$

and

$$\begin{aligned}\hat{L}^-(z_0) &= (R(z_0,z_1) + T(z_1,z_0)\boldsymbol{R}(z_0,z_1,z_2))\hat{L}^+(z_0)\\ &\quad + T(z_1,z_0)\boldsymbol{T}(z_2,z_1,z_0)\hat{L}^-(z_2)\\ &\quad + T(z_1,z_0)\boldsymbol{\Sigma}(z_2,z_1,z_0) + \Sigma(z_1,z_0),\end{aligned} \tag{E.13}$$

with coefficients equal to

$$\begin{aligned}T(z_0,z_2) &= T(z_1,z_2)(1-R(z_1,z_0)R(z_1,z_2))^{-1}T(z_0,z_1)\\ R(z_2,z_0) &= T(z_1,z_2)(1-R(z_1,z_0)R(z_1,z_2))^{-1}R(z_1,z_0)T(z_2,z_1) + R(z_2,z_1)\\ \Sigma(z_0,z_2) &= T(z_1,z_2)(1-R(z_1,z_0)R(z_1,z_2))^{-1}(R(z_1,z_0)\Sigma(z_2,z_1) + \Sigma(z_0,z_1))\\ &\quad + \Sigma(z_1,z_2)\\ R(z_0,z_2) &= R(z_0,z_1) + T(z_1,z_0)(1-R(z_1,z_2)R(z_1,z_0))^{-1}R(z_1,z_2)T(z_0,z_1)\\ T(z_2,z_0) &= T(z_1,z_0)(1-R(z_1,z_2)R(z_1,z_0))^{-1}T(z_2,z_1)\\ \Sigma(z_2,z_0) &= T(z_1,z_0)(1-R(z_1,z_2)R(z_1,z_0))^{-1}(R(z_1,z_2)\Sigma(z_0,z_1) + \Sigma(z_2,z_1))\\ &\quad + \Sigma(z_1,z_0).\end{aligned} \tag{E.14}$$

Appendix F. Solving the elastic-scattering RTE

For $\lambda' \mapsto \lambda$, $1 \le i \le M$ and $0 \le \ell \le N$ we have the spectral RTE

$$\begin{aligned}\tilde{\mu}_i \frac{d}{dz}L(z;\lambda;i;\ell) &= -c(z;\lambda)L(z;\lambda;i;\ell) + \sum_{\pm j=1}^{M}\beta_E(z;\lambda;i,j;\ell)L(z;\lambda;j;\ell)\\ &\quad + \sum_{\pm j=1}^{M}\int_{\Lambda}\beta_I(z;\lambda,\lambda';i,j;\ell)L(z;\lambda';j;\ell)d\lambda' + \sigma(z;\lambda;i;\ell)\end{aligned} \tag{F.1}$$

where $\beta_I(z;\lambda,\lambda';i,j;\ell)$ denotes the inelastic volume scattering function from wavelengths λ' to λ over a bounded λ-spectrum $\Lambda \subset \mathbb{R}_{>0}$. We introduce a notion of band averaging for functions $F(\lambda)$ by defining

$$F(m) := \frac{1}{\mathrm{Vol}(\Lambda_m)}\int_{\Lambda_m} F(\lambda)d\lambda \tag{F.2}$$

for a closed interval $\Lambda_m \subset \Lambda$. For functions of two variables $G(\lambda,\lambda')$ and another closed interval, $\Lambda_n \subset \Lambda$ we define

$$G(m,n) := \frac{1}{\mathrm{Vol}(\Lambda_m)}\int_{\Lambda_m}\int_{\Lambda_n} G(\lambda,\lambda')d\lambda' d\lambda. \tag{F.3}$$

Assuming that inelastic scattering β_I is compactly supported with respect to λ' we may band average over a union of intervals $\Lambda = \bigcup_{n=1}^{B} \Lambda_n$ (F.1) so that

$$\tilde{\mu}_i \frac{d}{dz} L(z; m; i; \ell) = \sum_{\pm j=1}^{M} \sum_{n=1}^{B} (\beta_E(z; m; i, j; \ell) - c(z; m)\delta_{i,j})\delta_{m,n} L(z; n; j; \ell) + \sum_{\pm j=1}^{M} \sum_{n=1}^{B} \beta_I(z; m, n; i, j; \ell) L(z; n; j; \ell) + \sigma(z; m; i; \ell) \tag{F.4}$$

References

Online References. All references to online media quoted by hyperlink/web address are correct up to the last date of observation on 16th February 2022.

[1] V. Ambarzumian, Diffuse Reflection of Light by a Foggy Medium, vol. 38, C. R. (Doklady) Acad. Sci. URSS (N.S.), 1943, pp. 229–232.

[2] S. Bazeille, I. Quidu, L. Jaulin, Identification of underwater man-made object using a colour criterion, in: Conference on Detection and Classification of Underwater Targets, 2007, hal–00504885.

[3] R. Bellman, G. Wing, An Introduction to Invariant Imbedding, vol. 8, Society for Industrial and Applied Mathematics (SIAM), 1975, http://dx.doi.org/10.1137/1.9781611971279.

[4] L. Bohan, L. Zhaojun, M. Shaojie, L. Yongfu, D. Zhongjun, H. Jiahao, Z. Zhigang, Underwater hyperspectral imaging technology and its applications for detecting and mapping the seafloor: A review, Sensors 20 (17) (2020) http://dx.doi.org/10.3390/s20174962.

[5] A. Bricaud, A. Morel, M. Babin, K. Allali, H. Claustre, Variations of light absorption by suspended particles with chlorophyll a concentration in oceanic (case 1) waters: Analysis and implications for bio-optical models, J. Geophys. Res. 103 (C13) (1998) 31033–31044, http://dx.doi.org/10.1029/98JC02712.

[6] H. Buiteveld, J. Hakvoort, M. Donze, Optical properties of pure water, in: J. Jaffe (Ed.), in: Ocean Optics XII, vol. 2258, International Society for Optics and Photonics, SPIE, 1994, pp. 174–183, http://dx.doi.org/10.1117/12.190060.

[7] K. Chance, R. Kurucz, An improved high-resolution solar reference spectrum for earth's atmosphere measurements in the ultraviolet, visible, and near infrared, J. Quant. Spectrosc. Radiat. Transfer 111 (9) (2010) 1289–1295, http://dx.doi.org/10.1016/j.jqsrt.2010.01.036.

[8] A. Corbett, D. Kangin, Imbedding deep neural networks, in: 10th International Conference on Learning Representations, ICLR, 2022, URL https://openreview.net/forum?id=yKIAXjkJc2F.

[9] D. D'Alimonte, G. Zibordi, T. Kajiyama, J. Cunha, Monte Carlo code for high spatial resolution ocean color simulations, Appl. Opt. 49 (26) (2010) 4936–4950, http://dx.doi.org/10.1364/AO.49.004936.

[10] E. Darles, B. Crespin, D. Ghazanfarpour, J. Gonzato, A survey of ocean simulation and rendering techniques in computer graphics, Comput. Graph. Forum 30 (1) (2011) 43–60.

[11] G. Fournier, J. Forand, Analytic phase function for ocean water, in: Jules S. Jaffe (Ed.), Ocean Optics XII, vol. 2258, International Society for Optics and Photonics, SPIE, 1994, pp. 194–201, http://dx.doi.org/10.1117/12.190063.

[12] F. Frank M. Sogandares, E. Fry, Absorption spectrum (340–640 nm) of pure water. I. Photothermal measurements, Appl. Opt. 36 (33) (1997) 8699–8709, http://dx.doi.org/10.1364/AO.36.008699.

[13] V. Haltrin, Chlorophyll-based model of seawater optical properties, Appl. Opt. 38 (33) (1999) 6826–6832, http://dx.doi.org/10.1364/AO.38.006826.

[14] L. Henyey, J. Greenstein, Diffuse radiation in the galaxy, Astrophys. J. 93 (1941) 70–83, http://dx.doi.org/10.1086/144246.

[15] H. Huang, Z. Sun, S. Liu, Y. Di, J. Xu, C. Liu, R. Xu, H. Song, S. Zhan, J. Wu, Underwater hyperspectral imaging for in situ underwater microplastic detection, Sci. Total Environ. 776 (2021) 145960, http://dx.doi.org/10.1016/j.scitotenv.2021.145960.

[16] N. Igawa, Y. Koga, T. Matsuzawa, H. Nakamura, Models of sky radiance distribution and sky luminance distribution, Sol. Energy 77 (2) (2004) 137–157, http://dx.doi.org/10.1016/j.solener.2004.04.016.

[17] N. Jerlov, Optical oceanography, in: Elsevier oceanography series, vol. 5, Elsevier Pub. Co., 1968.

[18] G. Johnsen, Z. Volent, H. Dierssen, R. Pettersen, M. Van Ardelan, F. Søreide, P. Fearns, M. Ludvigsen, M. Moline, Underwater hyperspectral imagery to create biogeochemical maps of seafloor properties, in: J. Watson, O. Zielinski (Eds.), Subsea Optics and Imaging, in: Woodhead Publishing Series in Electronic and Optical Materials, Woodhead Publishing, 2013, pp. 508–540e, http://dx.doi.org/10.1533/9780857093523.3.508.

[19] L. Johnson, R. Green, M. Leeson, Underwater optical wireless communications: Depth dependent variations in attenuation, Appl. Opt. 52 (33) (2013) 7867–7873, http://dx.doi.org/10.1364/AO.52.007867.

[20] M. Lewis, J. Cullen, T. Platt, Phytoplankton and thermal structure in the upper ocean: Consequences of nonuniformity in chlorophyll profile, J. Geophys. Res. 88 (1983) 2565–2570, http://dx.doi.org/10.1029/JC088iC04p02565.

[21] C.-C. Liu, J. Woods, Prediction of ocean colour: Monte Carlo simulation applied to a virtual ecosystem based on the Lagrangian ensemble method, Int. J. Remote Sens. 25 (5) (2004) 921–936, http://dx.doi.org/10.1080/0143116031000139809.

[22] H. Loisel, A. Morel, Light scattering and chlorophyll concentration in case 1 waters: A reexamination, Limnol. Oceanogr. 43 (5) (1998) 847–858, http://dx.doi.org/10.4319/lo.1998.43.5.0847.

[23] C. Mobley, Light and Water, Academic Press, 1994.

[24] C. Mobley, Polarized reflectance and transmittance properties of windblown sea surfaces, Appl. Opt. 54 (17) (2015) 5392–5401, http://dx.doi.org/10.1364/AO.54.005392.

[25] C. Mobley, E. Boss, C. Roesler, Ocean Optics Web Book, Academic Press, 2021, URL https://www.oceanopticsbook.info.
[26] A. Morel, D. Antoine, B. Gentili, Bidirectional reflectance of oceanic waters: Accounting for Raman emission and varying particle scattering phase function, Appl. Opt. 41 (30) (2002) 6289–6306, http://dx.doi.org/10.1364/AO.41.006289.
[27] N. Ohta, The Basis of Color Reproduction Engineering, Corona-sha Co, Japan, 1997, (in Japanese).
[28] W. Pegau, Deric Gray, J. Zaneveld, Absorption and attenuation of visible and near-infrared light in water: Dependence on temperature and salinity, Appl. Opt. 36 (1997) 6035–6046, http://dx.doi.org/10.1364/AO.36.006035.
[29] R. Perez, P. Ineichen, R. Seals, J. Michalsky, R. Stewart, Modeling daylight availability and irradiance components from direct and global irradiance, Sol. Energy 44 (5) (1990) 271–289, http://dx.doi.org/10.1016/0038-092X(90)90055-H.
[30] T. Petzold, Volume scattering functions for selected ocean waters, Scr. Inst. Oceanogr. 32 (1972) 72–78, http://dx.doi.org/10.1364/AO.32.007484, SIO Ref.
[31] T. Platt, S. Sathyendranath, Oceanic primary production: Estimation by remote sensing at local and regional scales, Science 241 (4873) (1988) 1613–1620, http://dx.doi.org/10.1126/science.241.4873.1613.
[32] R. Pope, E. Fry, Absorption spectrum (380–700 nm) of pure water. II. integrating cavity measurements, Appl. Opt. 36 (33) (1997) 8710–8723, http://dx.doi.org/10.1364/AO.36.008710.
[33] R. Smith, K. Baker, Optical properties of the clearest natural waters (200–800 nm), Appl. Opt. 20 (2) (1981) 177–184, http://dx.doi.org/10.1364/AO.20.000177.
[34] M. Solonenko, C. Mobley, Inherent optical properties of jerlov water types, Appl. Opt. 54 (17) (2015) 5392–5401, http://dx.doi.org/10.1364/AO.54.005392.
[35] J. Tou, Modern Control Theory, McGraw–Hill, 1964.
[36] J. Uitz, H. Claustre, A. Morel, S. Hooker, Vertical distribution of phytoplankton communities in open ocean: An assessment based on surface chlorophyll, J. Geophys. Res. 111 (C8) (2006) http://dx.doi.org/10.1029/2005JC003207.